

High-speed dual Langmuir probe

Robert B. Lobbia and Alec D. Gallimore

*Department of Aerospace Engineering, Plasmadynamics and Electric Propulsion Laboratory,
The University of Michigan, Ann Arbor, Michigan 48109, USA*

(Received 24 November 2009; accepted 23 May 2010; published online 15 July 2010)

In an effort to temporally resolve the electron density, electron temperature, and plasma potential for turbulent plasma discharges, a unique high-speed dual Langmuir probe (HDLP) has been developed. A traditional single Langmuir probe of cylindrical geometry (exposed to the plasma) is swept simultaneously with a nearby capacitance and noise compensating null probe (fully insulated from the plasma) to enable bias sweep rates on a microsecond timescale. Traditional thin-sheath Langmuir probe theory is applied for interpretation of the collected probe data. Data at a sweep rate of 100 kHz are presented; however the developed system is capable of running at 1 MHz—near the upper limit of the applied electrostatic Langmuir probe theory for the investigated plasma conditions. Large sets (100 000 sweeps at each of 352 spatial locations) of contiguous turbulent plasma properties are collected using simple electronics for probe bias driving and current measurement attaining 80 dB signal-to-noise measurements with dc to 1 MHz bandwidth. Near- and far-field plume measurements with the HDLP system are performed downstream from a modern Hall effect thruster where the time-averaged plasma properties exhibit the approximate ranges: electron density n_e from (1×10^{15}) – (5×10^{16}) m⁻³, electron temperature T_e from 1 to 3.5 eV, and plasma potential V_p from 5 to 15 V. The thruster discharge of 200 V (constant anode potential) and 2 A (average discharge current) displays strong, 2.2 A peak-to-peak, current oscillations at 19 kHz, characteristic of the thruster “breathing mode” ionization instability. Large amplitude discharge current fluctuations are typical for most Hall thrusters, yet the HDLP system reveals the presence of the same 19 kHz fluctuations in $n_e(t)$, $T_e(t)$, and $V_p(t)$ throughout the entire plume with peak-to-peak divided by mean plasma properties that average 94%. The propagation delays between the discharge current fluctuations and the corresponding plasma density fluctuations agree well with expected ion transit-times observed with distinct plasma waves traveling away from the thruster at velocities >10 km/s. © 2010 American Institute of Physics. [doi:10.1063/1.3455201]

I. INTRODUCTION

Langmuir probes were the first plasma diagnostic¹ developed nearly a century ago. Today they are still employed as one of the most useful and common means of measuring plasma density, electron temperature [or the electron energy distribution function (EEDF)], plasma potential, or floating potential with excellent spatial resolution, and a simple theory of probe data interpretation.^{2–5} The temporal resolution of this indispensable electrostatic diagnostic has often been quoted as the inverse of the ion plasma frequency,^{3,4} which should enable microsecond resolution for a variety of plasmas. In a companion paper to this work, the temporal resolution of a rapidly swept Langmuir probe [and in high-speed dual Langmuir probe (HDLP) configuration] was examined in detail confirming submicrosecond resolution (limited, not just by f_{pi}^{-1} , but by capacitive and polarization effects) for plasma environments typical to Hall effect thrusters (HETs) and tokamaks.⁶ In this work the developed HDLP diagnostic is detailed and typical time- and space-resolved data taken downstream from a modern HET thruster are presented.

A. Background: Rapid sweep Langmuir probing

A scattering of previous investigations of rapidly swept (faster than or equivalent to 100 kHz) Langmuir probe experiments^{7–11} has met limited success due to the many challenges of such measurements—most stemming from the electrical biasing and measurement circuits. Cabling and circuit stray capacitance can introduce displacement current that can easily exceed the electron saturation current and some means of compensating for this current is required. The use of a capacitance matched “dummy probe” was first suggested by Chen⁴ in 1966, and various implementations of this have utilized an external (positioned far from the actual Langmuir probe) but otherwise similar probe^{9,10,12} or a variable capacitor.^{7,11} Perhaps the largest flaw of all prior fast-sweep Langmuir probe experiments resides in the use of low 8–12 bit digitization common to oscilloscope and high-speed data acquisition (DAQ) cards. Coupled to small sample-set sizes (often less than 100 consecutive I - V curves), low-precision measurements are nearly unavoidable. In the high-speed dual Langmuir probe (HDLP) presented here, a null or dummy probe is used also, but effort was made to ensure the probes, and all circuitry and their wiring remained within 1

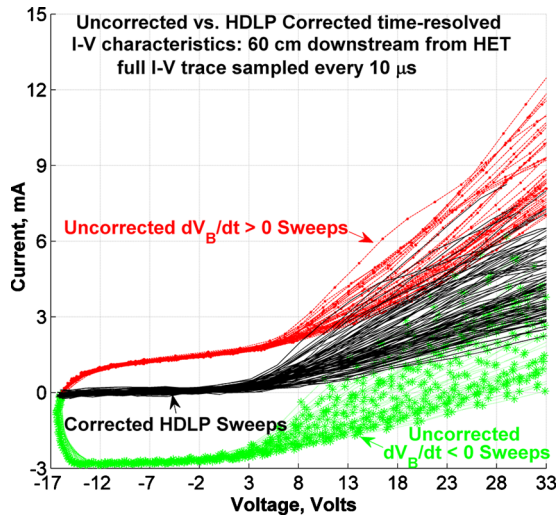


FIG. 2. (Color online) 100 time-resolved I - V characteristics acquired at 100 kHz showing the use of Eq. (1) for HDLP data 60 cm downstream of the HET discharge channel exit.

ms of HET plume data collection. The corrected I - V traces are devoid of cable capacitive effects and the wide family of I - V curves at this single point indicates strong plasma fluctuations arising for the HET breathing mode phenomena. Rounding of the uncompensated I - V space profiles occurs at the bias voltage range edges due to the change of sign in dV_B/dt and finite frequency-response effects.

B. Probe transmission lines

In an effort to minimize line capacitance along the conduction path from the probes to the bias driving amplifier, high-speed transmission line characteristics were studied in conjunction with SPICE circuit simulation software. Conventional Langmuir probe wiring consists of fully shielded coaxial cable or twisted pair cable—yet with respective capacitances of 100 and 50 pF/m, use of these lines would have led to the generation of displacement currents at least two orders of magnitude larger than the expected far-field electron saturation current. Indeed, simulations involving large capacitive loading on the bias amplifier caused circuit destabilization in many scenarios. This phenomenon necessitated either placement of all circuitry (amplifier and current sensors) inside the chamber (in close proximity to the Langmuir and null probes) or the use of dramatically lower capacitance transmission lines.

The theoretical capacitance per meter from a single bare wire of conductor radius, r , suspended a height, h , over a ground plane can be determined from Gauss' law as $C_{||gnd} \approx 2\pi\epsilon_o/\ln(2h/r)$, where ϵ_o is the permittivity of free space. Thus, a small gauge wire suspended relatively far from any conductive grounding planes will possess a very low capacitance. In this experiment an 18-AWG stranded high-voltage silicone-insulated wire ($r_{18AWG}=0.5$ mm) along with fiberglass supporting posts are used to maintain a suspension height of $h \approx 0.3$ m for the cable runs inside and outside the vacuum chamber. The theoretical transmission line capacitance of this configuration is 8 pF/m. This estimate neglects the capacitance at the feedthroughs as well as

TABLE I. Specifications of the probe bias amplifier design for the HDLP.

Broadband power amplifier specifications	
Bandwidth	dc–1 MHz (–3 dB)
Voltage output	± 200 V
Current output	± 200 mA (four quadrants)
Voltage gain	20–40 dB

that inherent to the amplification and sensing circuitry. Measured total stray capacitance averages roughly 200–300 pF/probe, which varies from position to position and depends on the probe bias (via the plasma sheath surrounding the non-conductive portion of the probe support). This amount of stray capacitance works out to about 2–3 mA of displacement current for the 100 kHz swept data herein discussed and capacitive offsets of this magnitude are visible in Fig. 2. The ion and electron saturation currents at the furthest point from the thruster (64 cm) average about 1 μ A and 0.3 mA, respectively.

C. Probe biasing circuit

Conventional laboratory power supplies are not suitable for rapid high-voltage bias waveform generation since these supplies' frequency responses reside in the low kilohertz. In fact, there is a near void of commercially available high-voltage high-frequency broadband power-amplifiers that meet the requirements of the HDLP. SPICE was used to design a HDLP-capable amplifier with the specifications in Table I.

At the heart of the amplifier resides an APEX high-voltage (450-V) high-slew rate (1 kV/ μ s) metal-oxide-semiconductor field-effect transistor operational amplifier (PA98). Both active and passive coolings are applied to maintain stable high-performance operation (amplifier core temperature is continually monitored). Laboratory-grade switch-mode power supplies (<0.1% ripple) are employed as ± 220 V rails with significant bypassing to ensure low-noise amplification. Input to the PA98 is buffered, low-pass filtered (to about 1 MHz), and saturation-limited by a low-noise unity-gain operated Linear Technologies (LT1215) operational amplifier.

The biasing waveform provided as input (for presented data) is a 7.0 V peak-to-peak (or 70 V_{p-p} after amplification) 50 kHz symmetric triangle (or sawtooth) wave setup by a 20 MHz arbitrary waveform generator (Agilent 33220A). A slight dc offset of 15 V is applied to ensure the probe bias attains plasma potential and electron saturation current. Many experimentalists make use of a skewed ramping triangle waveform, taking swept I - V data only during the wider (often positive dV/dt) portions. However, the narrow (often subnanosecond wide) resetting of such waveforms produces enormous voltage slew rates that would (if the amplifier could handle such loading) produce amperes of capacitively displaced current.

With the null probe capacitance correction, both halves of a symmetric triangle wave yield I - V characteristics in a manner more amenable to the plasma probe-sheath equilibrium since the monolithic bias ramping between ion and

electron saturations (then back to ion saturation, and so on) is not as abrupt as the skewed sawtooth. In this way, a 50 kHz triangle wave creates a full I - V characteristic, $V_B \in [-20 \text{ V}, 50 \text{ V}]$, every 10 μs , with interpreted plasma properties time-stamped at the center of each trace, which typically occurs when the bias is near the plasma potential.

D. Dual symmetric current sensing circuit

While shunt-based current measurement is typically a straightforward means to acquire small and large currents alike, the high-voltage and high-bandwidth contents of the Langmuir and null probe signals complicate this method of current measurement considerably. Ideally, the voltage drop across a shunt resistor can be amplified by an optically isolated analog amplifier, thereby removing the high common mode voltage (200 V or more) from the signal. Unfortunately, the frequency responses of the fastest modern isolation analog amplifiers cut off at 100–200 kHz, and for this experiment, 10 MHz or higher was targeted. Additionally, many conventional shunts are wire-wound precision resistors, which dissipate the I^2R heat load efficiently to minimize thermal resistance drifting. However, the inductance of wire-wound resistors is not negligible at high-frequencies greater than 1 MHz. Thankfully, a new class of thin- and thick-film metal oxide shunts is available with ultralow inductance and integrated heat sinks to maintain low thermal drifting. A BK Precision 5491A 50 000-count digital-multimeter was used to measure the shunt resistances with high accuracy, allowing for selection of a pair of well matched shunts, having nearly equivalent resistances, i.e., $<0.1\%$ different. The 5491A was also used to measure the high-precision (0.1% tolerance) resistors used in the construction of the -21 dB (1/11) voltage dividing networks (used here to reduce the high common mode voltages to a DAQ compatible range of $\pm 10 \text{ V}$). In order to keep the voltage division reductions constant, special high-bandwidth (dc to 20 MHz) ultrahigh input impedance junction field-effect transistor buffers were employed to maintain picoampere scale loading on the voltage dividing network. Current drain from the dividing networks may be corrected for during postprocessing, and using Fig. 1 with Ohm's law, Eq. (2) is obtained,

$$I_{LP,null}(t) = \frac{V_{IN}(t) - V_{B,null}(t)}{R_{S,LP,null}} - \frac{V_{B,null}(t)}{110 \text{ k}\Omega}. \quad (2)$$

Since here $R_S = 989.2 \text{ }\Omega \ll 110 \text{ k}\Omega$, the latter term can usually be ignored at a loss of accuracy. Using Eqs. (1) and (2), with measurement uncertainties of $\partial V_B = \pm 74 \text{ mV}$ [this includes analog-to-digital conversion (ADC) and divider network uncertainties] and $\partial R_S = \pm 0.1 \text{ }\Omega$, the typical current measurement overall accuracy is propagated to $\pm 53 \text{ }\mu\text{A}$ (average conditions). If DAQ channels are in short supply, the symmetric sensor design using identical current sensing shunts (i.e., $R_S = R_{S,LP} = R_{S,null}$) provides a good estimate of the true plasma current as simply $I_p \approx (V_{null} - V_{LP})/R_S$.

Often, with repeatable signals at high-frequencies, trigger aligned windowed averaging is a useful feature of oscilloscopes and DAQ systems that can dramatically increase the SNR (by up to \sqrt{N} , where N is the number of windows). Other electrostatic probe based investigations¹³ of HET

TABLE II. Specifications of the dual symmetric current sensing circuit designed for the HDLP.

Dual symmetric current sensing circuit specifications	
Bandwidth	dc–1 MHz (-3 dB) ^a
Measurement range	$\pm 200 \text{ mA}$ ^b
Resolution (with 16-bit DAQ)	3 μA
SNR (after DAQ)	80 dB
Max signal voltage	$\pm 150 \text{ V}$ ^b
Overall accuracy	$\pm (0.5\% \text{ reading} + 50 \text{ }\mu\text{A})$

^aIntentionally low-pass filtered match of the DAQ Nyquist frequency; unfiltered response is closer to dc–10 MHz.

^bThese limits are adjustable depending on choice of shunt and dividing network resistors.

plume transients have used this approach with limited success. The plasma in the plume of a HET is rich with turbulent fluctuations and this stochastic behavior invalidates this type of time-series ensemble averaging. For this experiment, extreme care was placed in minimizing signal noise. First, as mentioned in Sec. II, the null probe signal subtraction effectively removes noise picked up by the probe transmission lines. Second, the current sensing circuit was designed with two channels of symmetrically mirrored component and trace layouts. The circuitry was also shielded from the high-voltage transmission lines. The unshielded transmission lines act as antennas and volts of electromagnetic radiation can easily be picked up by any conductor in close proximity. The two matched low-noise current shunts are also thermally equalized to each other and ambient conditions via a large copper heat sink. An extra set of buffers provides additional output signal conditioning allowing for impedance matching with the coaxial cable connections to the DAQ system. The full measured specifications of the dual symmetric current sensing circuit are shown in Table II.

The noise level (measured with both a dummy resistive load and with an open circuit) in the sensed current is bounded in an envelope 20 μA wide. Since ion saturation currents (of the probe and plume investigated) are in the range of 1–50 μA , use of the electron saturation current (and not the ion saturation) for plasma density determination is required here as is typical for the HDLP approach.⁶ To prevent aliasing, the shunt resistors selected were chosen (in part) to form a low-pass filter with the probe transmission lines with a -3 dB cutoff frequency at $f_{RC} = 1/(2\pi C_S R_S) \approx 1 \text{ MHz}$, corresponding to the ADC Nyquist frequency.

E. I - V trace “noise” vanishing act

In all plasma measurements, whether from Langmuir probe characteristics or laser-induced fluorescence intensities, noise is omnipresent and often comparable to signal magnitudes in unfiltered signals. In many cases, this noise is the signature of high-speed transient plasma fluctuations such as the Hall thruster breathing mode. Common practice for plasma measurements incorporates extensive application of analog low-pass filters (inline additions or those built into low-frequency analog-to-digital converters), or postprocessing techniques such as boxcar averaging, smoothing, or more

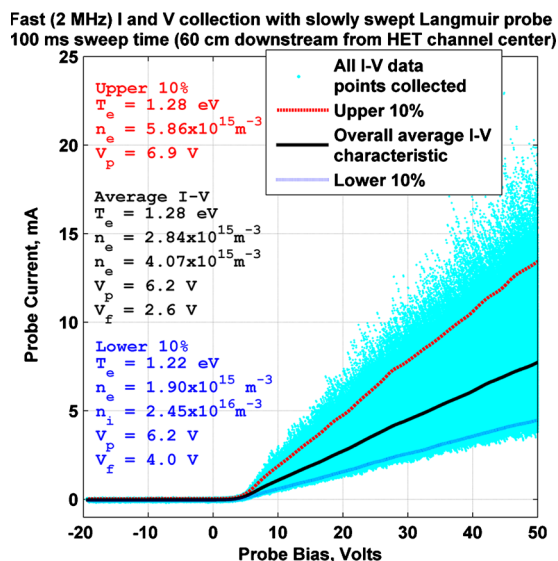


FIG. 3. (Color online) Misleading I - V noise observed for a slowly swept (100 Hz sweep rate) Langmuir probe taken 60 cm downstream of the HET (far-field). The raw I - V data pairs are sampled at 2 MHz and their resulting scatter is an indication not of poor measurement technique (the SNR = 80 dB here), but of plasma turbulence. A few averaged I - V traces are fitted to the raw I - V distributions to emphasize the arbitrariness of using the time-averaged I - V characteristic.

advanced digital signal processing methods (finite impulse response filters, infinite impulse response filters, etc.).

Once the rate of plasma property probing exceeds the rate of large scale plasma oscillations by more than twice, a vast majority of the noise simply vanishes. For Langmuir probe characteristics, this dramatic vanishing act is displayed by comparing Figs. 2 and 3 for two sweep rates: 100 Hz and 100 kHz. The same electronics and plasma environment give rise to rather distinct I - V characteristics each with varying degrees of noise. At 100 kHz, the I - V traces are individually quite smooth, while the 100 Hz swept I - V data are riddled with noise that arises from 19 kHz HET breathing mode turbulent plasma property fluctuations. The resolving of I - V noise as meaningful plasma transients is rather remarkable and with the HDLP I - V data, direct (unsmoothed) second-derivatives of the electron current are possible providing the capability to acquire time-resolved EEDFs using the HDLP.

F. HET plume

HDLP measurements are performed within the cylindrical (6-m diameter and 9-m long) stainless steel clad Large Vacuum Test Facility at the University of Michigan. A high-vacuum pressure of $<7 \times 10^{-6}$ torr (corrected for Xe) is maintained with 4 LN_2 baffled cryopanel throughout operation of the 600 W Hall thruster used in this study. The low-power thruster is fixed (near chamber centerline) to a thrust stand at one end of the cylindrical chamber and set to a nominal xenon discharge of 200 V, 2 A, and 5 mg Xe/s. Breathing mode oscillations¹⁴ are observed at all discharge settings for nearly all Hall type electric thrusters. However, at this lower voltage setting, the frequency of the oscillations apparent in the discharge current signal is near 20 kHz, and plasma measurements resolved at a rate of 100 kHz will

provide a relative abundance of HDLP samples per breathing cycle (compared to a 300 V discharge where this thruster breathing mode is about 40 kHz).

A graphite beam dump at the opposing end of the chamber receives the exhausted ions and helps reduce backscatter. The Langmuir and null probes are supported in a plane intersecting thruster centerline with a thin alumina (3.2 mm o.d. and 18 cm length) and aluminum/steel (with grafoil shielding) arm attached to pair of motion tables (1.45 m below the thruster axis) with a planar positioning range of 0–1 m axially and 0–1 m radially (see Fig. 1). While vibrations are minimal, an additional delay of 10 s is set between table motion and DAQ—thereby eliminating support or wiring induced motion effects that might otherwise yield false transient data in regions with strong plasma gradients.

After conditioning of the thruster (including at least 30 min of warm-up time at fixed discharge settings), automation of the table motion and DAQ is initiated with digital communication established between a set of three personal computers (PCs). 1 s of 2 MHz 16-bit ADC is recorded simultaneously for each of four DAQ channels (three for Langmuir and Null probe currents and voltages and one for thruster discharge current) at each of 352 grid-points throughout a 31×50 cm² planar region.

G. Signal processing

In anticipation of turbulent flow fluctuation analysis, large seamless multimillion element raw analog sample-sets are collected at each plume grid-point. Namely, 100 000 full I - V traces are conducted back-to-back over 1 s to ensure the gathering of enough information regarding the turbulent flow statistics. ADC data are moved from computer random access memory to hard-disk while the motion tables move the probes to the next interrogation point. Complete postprocessing of these data is computationally intensive, requiring in excess of 100 h to process 352 grid-points (20 Gbytes of binary data) with a 64-bit operating system on an 8-core 3 GHz PC. About 4000 lines of parallelized MATLAB code were written to perform this postprocessing.

The first task, after converting raw binary data into respective probe voltages and currents, is to remove the stray capacitance current (and EMI) from the Langmuir probe signal. This step entails a direct point-by-point subtraction of the Null probe measured current from the Langmuir probe measured current at each $0.5 \mu\text{s}$ time-step, using Eqs. (1) and (2). The time-resolved plasma properties are determined using a developed MATLAB script capable of processing about 300 I - V characteristics per second. Corrected probe plasma current and voltage signals are chopped into individual I - V trace sets (with one or two edge points clipped out and symmetry correction applied) and time-stamped at their center. The I - V characteristics are then interpreted using standard collisionless nonmagnetized thin-sheath Langmuir probe theory found in most texts¹⁻⁵ and outlined specifically for the HDLP in a companion paper⁶ to this work. Typical results from the Langmuir probe algorithm are shown in Fig. 4, while the time-resolved EEDF is included and appears quite Maxwellian (for this case; other cases are often markedly non-Maxwellian), the poor energy resolution

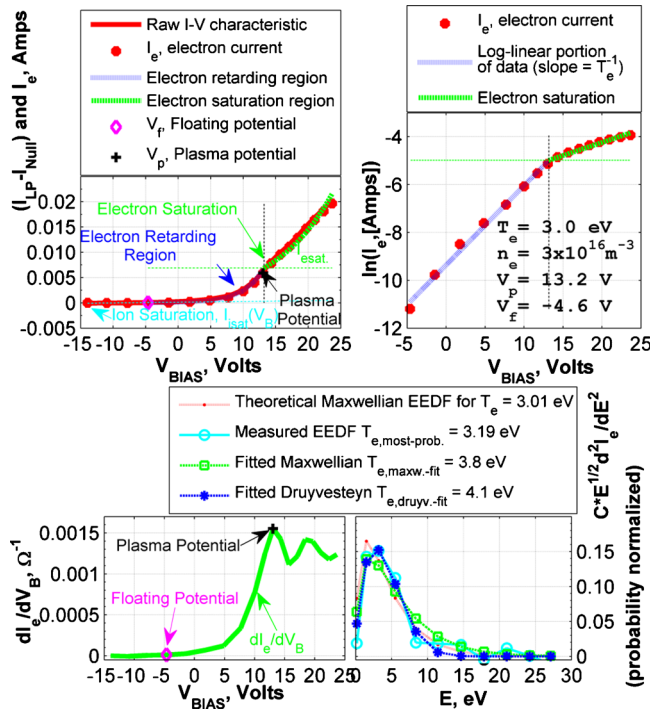


FIG. 4. (Color online) Typical single time-resolved (10 μ s) HDLP I - V characteristic with Langmuir probe algorithm results. The first and second electron current derivatives used in generating the lower two plots have not been smoothed and are computed numerically.

($\Delta E \approx 3$ eV) limits the usefulness and accuracy of EEDFs for the presented data. A future publication is currently being written that focuses on HDLP attained time-resolved EEDFs.

H. Error analysis

It is important to point out a shortcoming in the presented HDLP data involving the poor bias voltage (per single trace) resolution. The analog $I(t)$ and $V(t)$ sampling at 2 MHz captures only 20 points in I - V space per single time-resolved trace. This creates gaps of 1–4 V between consecutive bias voltage samples—fundamentally increasing uncertainty in the measurement of $V_f(t)$ and $V_p(t)$, but not necessarily $T_e(t)$ (using inverse slope method) or $n_e(t)$. While linear (or spline) interpolation between points reduces the error in computing $V_f(t)$, the uncertainty in $V_p(t)$ and the energy resolution of an EEDF remain about equal to the spacing of the bias voltage points [since $V_p(t)$ and the EEDF are based on nonconstant derivatives with respect to probe bias]. Propagation of all measurement errors (prefixed with ∂) is performed in the conventional manner taking special notice to the discrete nature of the ADC measurements. The uncertainty in plasma potential ∂V_p is estimated as a combination of the bias uncertainty and the discrete spacing between bias voltages, accounting for the voltage drop across the current sensing shunt, $\Delta V_{B,\text{step}}|_{V_B \approx V_p} = (\Delta V_B / N_B) T_e / (T_e + I_{\text{sat}} R_s)$, where N_B is the number of I - V samples spanning the total bias sweep range ΔV_B . For ∂T_e , the discrete form of the data is again considered along with averaged I - V values ranging from V_f to V_p ; it should be noted that nonsystematic T_e uncertainties are reduced by a factor of $1/\sqrt{N_{T_e}-1}$, with

N_{T_e} as the number of I - V points used in the determination of T_e . Thus is a collection of HDLP uncertainties presented in Eq. (3),

$$\begin{aligned} \partial A_p &= 2\pi \sqrt{(\partial r_p L_p)^2 + (r_p \partial L_p)^2}, \\ \partial V_B &= V_B \sqrt{\left(\frac{\partial F_{\text{div}}}{F_{\text{div}}}\right)^2 + \left(F_{\text{div}} \frac{\partial V_{\text{DAQ}}}{V_B}\right)^2}, \\ \partial I_p &\approx 2I_p \sqrt{\left(\frac{\partial V_B}{I_p R_s}\right)^2 + \left(\frac{\partial R_s}{R_s}\right)^2}, \\ \partial T_e &\approx T_e \sqrt{2\left(\frac{\partial V_B}{\Delta V_{B,\text{step}}}\right)^2 + 8\left(\frac{T_e \partial I_p}{\Delta V_{B,\text{step}} I_{\text{sat}}}\right)^2}, \\ \partial n_e &\approx n_e \sqrt{\left(\frac{\partial I_p}{I_{\text{sat}}}\right)^2 + \left(\frac{\partial A_p}{A_p}\right)^2 + \left(\frac{\partial T_e}{2T_e}\right)^2}, \\ \partial V_p &\approx \sqrt{(\partial V_B)^2 + (\Delta V_{B,\text{step}})^2}, \\ \partial V_f &\approx \sqrt{(\partial V_B)^2 + \left(T_e \frac{\partial I_p}{I_{\text{sat}}}\right)^2}. \end{aligned} \quad (3)$$

Equation (3) introduces voltage divider network uncertainty $\partial F_{\text{div}} = \pm 0.014$ (for $F_{\text{div}} = 11$), probe area uncertainty $\partial A_p = \pm 0.6 \times 10^{-6}$ m² (for a cylindrical probe of radius $r_p = 0.25$ mm and length $L_p = 3.1$ mm), and $\partial V_{\text{DAQ}} = \pm 2$ mV. In Eq. (3), units are International System of Units except for electron temperature in eV. While these uncertainty estimates vary throughout the plume, the relative uncertainties for the data in this article range approximately $\partial n_e / n_e \approx \partial T_e / T_e \approx 10\% - 20\%$ and $\partial V_p / V_p = 10\% - 40\%$. It is worthwhile to note that the uncertainties in Eq. (3) are not inclusive of uncertainties inherent to the applied sheath-limited electrostatic probe theory (typically on the order of 50%). Indeed, as derived in the examination of the HDLP temporal limits,⁶ a barrage of additional dynamic effects (sheath displacement current, polarization drift current, etc.) is known to adversely affect the collected plasma current. For the conditions of this experiment these effects are anticipated to contribute additional collected current $|\Delta I_{\text{dyn}}|$, on the order of the ion saturation current. Since $|\Delta I_{\text{dyn}}| \leq |I_{\text{sat}}| \ll \partial I_p$ for this work, the above equations are largely unaffected, but the accuracy of the floating potential is quite low. Using the slope of the (Maxwellian) electron current near the floating potential one obtains the final term of the final line of Eq. (3), $\partial V_f|_{\text{from } \partial I_p} \approx \partial I_p / (dI_p / dV|_{V_f})$. When $\partial I_p \approx |I_{\text{sat}}|$, the uncertainty in the floating potential is then approximately $\partial V_f \approx \pm T_e$; however, for the data in this work, the uncertainty in the floating potential is many times the magnitude of T_e since $\partial I_p > |I_{\text{sat}}|$ at all locations.

Finally, validation of the HDLP was obtained by several methods. Using the same experimental setup to measure the same plume region and conditions, a slowly swept Langmuir probe (100 sweeps/s) provided time-averaged I - V traces (see black trace in Fig. 3). Plasma properties from these time-averaged I - V traces versus time-averaged properties from the HDLP (100 kHz) traces exhibit an average difference of about 23%. The subtleties involved in the differences such as

systematic underpredictions of electron temperature with the slowly swept Langmuir probe (whose I - V characteristics possess two distinct electron populations: hotter primary and cooler bulk groups) are under continued study and will be published in a future work. Second, the dynamics of the plasma was qualitatively validated by use of a high-speed (109 500 frames/s) camera that confirmed the existence of visible emission fluctuations from the plasma in direct proportion with the HDLP measurements.¹⁵

III. RESULTS

Large magnitude fluctuating plasma properties are measured throughout the entire 31×50 cm² plume region interrogated. The spatially and temporally averaged ratios of the fluctuation standard deviation (denoted with prefix δ) to the time-averaged property values (denoted by “ $\bar{}$ ”) work out to

$$\left\langle \frac{\delta n_e}{\bar{n}_e}, \frac{\delta T_e}{\bar{T}_e}, \frac{\delta V_p}{\bar{V}_p} \right\rangle_{31 \text{ by } 50 \text{ cm HET plume}} \approx 53.3\% \pm 9.8\%. \quad (4)$$

Strong cross-correlations of the fluctuations to each other and to the thruster discharge signal are evident in Fig. 5. The displayed oscillations originate from a natural relaxation mechanism¹⁶ established in the Hall thruster discharge channel (an approximately 1 cm deep annular cavity) known as the “breathing mode.” This low-frequency (19 kHz) oscillation causes the discharged current to increase dramatically during an ionization burst that sends a large flux of electrons to the 200 V anode positioned at the base of the discharge channel. The large burst of ionized propellant ions is then accelerated away from the anode and thruster thereby creating thrust oscillations (although not yet measured, must surely exist) as well as the fluctuating appearance of the electron density (as well as ion-density since $n_i \approx n_e$) and other plasma properties.

The assumption of quasineutrality is common for the discharge within the plume of a Hall thruster. However, closer examination of the emitted plasma density waves suggests the possible existence of double layers. In this manner, each burst of plasma may be surrounded by a sheath that could be acting to fundamentally alter thruster performance through electrostatic shielding coupled with plasma potential oscillations that are in or out of phase with the density fluctuations.

A. Ion transit delay

The delay between initial spikes in discharge current $I_D(t)$ and corresponding fluctuations in the electron density $n_e(t)$ (as in Fig. 5) quite accurately matches the expected ion transit-times for Xe⁺ ions originating from the thruster discharge channel. Generally, the bulk (>95%) of the ion acceleration occurs within two thruster diameters of a HET (mean channel diameter here is approximately 5 cm). As the precise length of the acceleration zone is unknown for this thruster, an estimate of the theoretical transit time, $\tau_{i,t}$, is

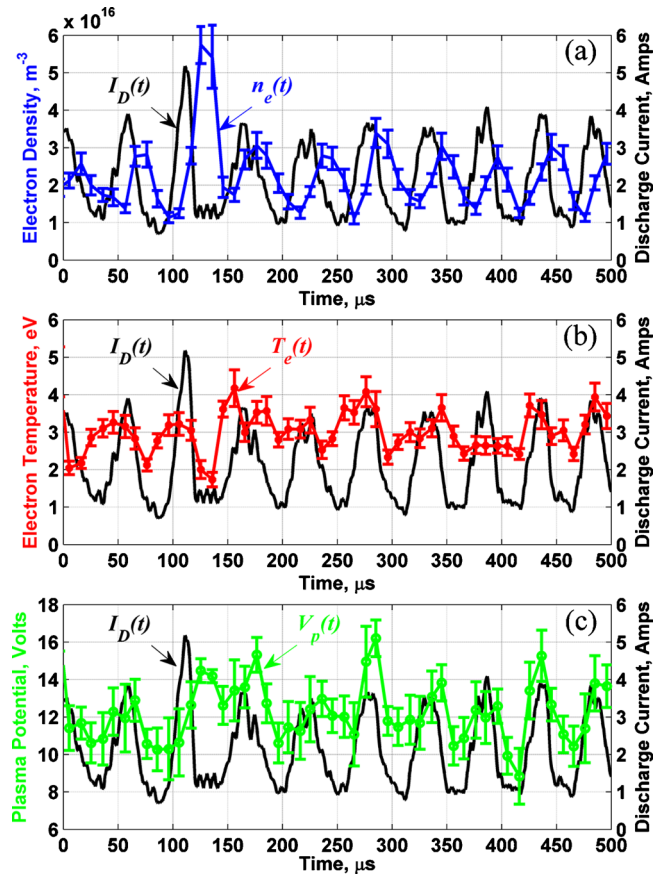


FIG. 5. (Color online) HDLP time-resolved simultaneous plasma properties measured 20 cm downstream (channel-aligned) from the HET. The black solid signal in (a)–(c) shows the instantaneous thruster discharge current $I_D(t)$ that is dominated by the 19 kHz breathing mode fluctuation. While electron density fluctuations (a) follow the $I_D(t)$ fluctuations with a short delay (≈ 20 μs), (b) $T_e(t)$ and (c) $V_p(t)$ track the fluctuations nearly in phase. This sequence is a small 0.5 ms portion typical of the 1 s of data collected at this position.

made as the integrated time to accelerate (in the axial direction x , with $x=0$ at the thruster exit plane) to the expected propellant ion velocity U_i (based on discharge potential V_D), in two thruster diameters plus the time at this speed to reach the point of interest,

$$\tau_{i,t}(x) = \frac{m_i U_i L_a}{e \eta_V V_D} + \frac{x - L_a}{U_i} = \frac{x + L_a}{U_i}, \quad x \geq L_a,$$

and

$$\frac{1}{2} m_i U_i^2 = e \eta_V V_D \rightarrow U_i = \sqrt{2e \eta_V V_D / m_i}. \quad (5)$$

A constant electric field is assumed throughout the acceleration zone ($L_a=10$ cm) with a voltage utilization efficiency (η_V) of 80% (for singly charged xenon ions with mass m_i and charge e). Thus at 20 cm downstream (as in Fig. 5) one finds $\tau_{i,t}(20 \text{ cm})=19.61$ μs.

By looking at the phase, ϕ_d , between the discretely transformed Fourier coefficients of the discharge current and electron density at the breathing mode frequency, f_B , one may compute an accurate (most statistically probable) value of this delay, τ_d , using Eq. (6),

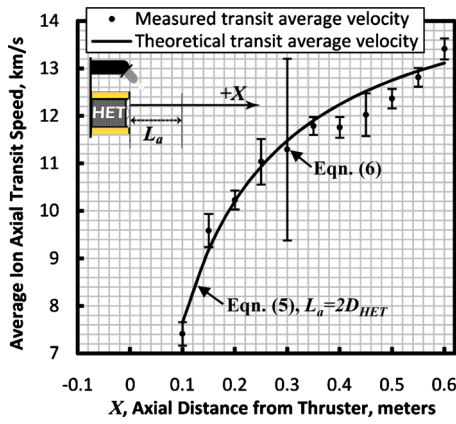


FIG. 6. (Color online) Average axial ion transit speeds, measured vs (1D) theoretically expected values. The “error-bars” included span the 95% confidence intervals of the phase measurements and thereby indicate the level of turbulent uncertainty in phase at each location.

$$\tau_d(x) = \frac{\phi_d(x)}{2\pi f_B}, \quad (6)$$

$$\tau_d(20 \text{ cm}) = \frac{130.7^\circ \pm 2^\circ}{360^\circ \times 18.6 \text{ kHz}} = 19.57 \pm 0.3 \text{ } \mu\text{s}.$$

The “uncertainty” in this phase measurement is taken as the 95% confidence interval for a narrow 100 Hz wide band about f_B . Since this phase measurement is taken as the effective average phase between about 19 000 breathing mode peaks in $I_D(t)$ and $n_e(t)$, the uncertainty here is an indirect measure of the turbulence level that causes some ion bursts to travel faster (–) or slower (+) than the most probable travel time. A proper estimate of measurement uncertainty is taken as the measurement resolution divided by the square-root of the number of samples: $10 \text{ } \mu\text{s} / \sqrt{19\,000} = \pm 0.07 \text{ } \mu\text{s}$. For this case at 20 cm downstream, the simple one-dimensional (1D) theory and phase measurement agree within 0.2%. For the entire axial profile ($x=10$ to 60 cm) aligned with the radial center ($r \approx 3$ cm) of the accelerating discharge channel Fig. 6 is constructed by dividing x by Eqs. (5) and (6) resulting in an average difference of 2.3%. The large turbulent uncertainty in phase apparent at 0.3 m downstream is likely caused by the initially toroidally shaped (inside the annular discharge channel) breathing mode ion wave achieving thermally expanded closure. Using the inner HET channel diameter (≈ 4 cm), Eq. (5) for average transit velocity ($\bar{U}_{i,t} = x / \tau_{i,t}$), and an average electron temperature of 2.9 eV closure (upon the channel-aligned x -axis in Fig. 6) should occur near $x_{\text{closure}} \approx D_{\text{inner,HET}} \bar{U}_{i,t} / U_{\text{Bohm}} = D_{\text{inner,HET}} \sqrt{2\eta_V V_D / T_e} - L_a = 0.32 \text{ m}$.

B. Electron temperature and plasma potential fluctuations

Comparing the instantaneous measurements of thruster discharge current, electron temperature, and plasma potential, a near zero phase difference in the breathing mode oscillations is seen. For the electron temperature one might expect the delay to be set by the electron thermal motion and for 3 eV bulk electrons traveling at over 1×10^6 m/s, this

delay ($\approx 0.2 \text{ } \mu\text{s}$, at 20 cm) is well under the $10 \text{ } \mu\text{s}$ temporal resolution of the HDLP system. Since the HET discharge circuit closes between the inner discharge channel anode and externally mounted cathode, the burst of ions generated with each breathing mode cycle produces an equivalent burst of electrons from the cathode. This in-rush demand for more electron current from the cathode may be met in part by increased electron heating inside the cathode (as well as inside the ionizing closed-drift Hall current), thereby generating the peaks in $T_e(t)$ (seen in Fig. 5) that occur nearly simultaneously with $I_D(t)$ peaks.

With each ionization burst, a rapid buildup of plasma density in a narrow localized region (with axial width on the order of ion-acoustic speed multiplied by the time from burst beginning or $U_{\text{Bohm}} t_b$) produces a pressure gradient pushing the more mobile (nonmagnetized in the plume) electrons outward into the surrounding space, a process that leads to a rapidly (again at electron thermal velocity) lowered plasma potential at distances downstream. However, it is not quite this simple because these electrons represent a hotter population and, if their thermal-pressure overcomes the density-pressure, then the plasma potential downstream of the ion burst would then increase to balance out the pressure with an electric field. From the data in Fig. 5, it seems that both effects may be occurring since not all the peaks in both $I_D(t)$ and $V_p(t)$ line up.

Another complicating effect that occurs once the density wave reaches a given downstream location is the convected properties of the plasma therein contained. It seems likely that the electrons carried by the wave may be cooler since the hotter ones are the first to react to the density-pressure losses, and this in combination with the potential set up to balance the density gradient pressure force leads to a higher plasma potential inside the traveling density wave. Altogether the electron physics here is not captured with the simple Boltzmann relation and a more complete description demanding perhaps an alternate form of the time-dependent (nonlinearized) Boltzmann equation is needed to understand the constantly shifting nature of electron equilibrium within this fluctuating plasma plume.

IV. CONCLUSIONS

A novel HDLP has been developed for achieving time-resolved measurements near the upper limit of electrostatic probe theory. A null probe, used to compensate for stray capacitive and EMI effects, proved key in enabling swept bias and plasma property collection rates of 100 kHz. Combined with carefully designed (yet simple) electronics and DAQ for making high SNR measurements, large magnitude (standard deviations 53% of the time-averaged values) plasma fluctuations—set up by the 19 kHz Hall thruster breathing mode oscillation—were observed at all spatial locations within a $31 \times 50 \text{ cm}^2$ planar downstream region. Density wave correlations with the thruster discharge current revealed delays that agree to within 2% of the theoretically expected ion transit time. Electron temperature and plasma potential fluctuations occur not just with the rapidly traveling ($>10 \text{ km/s}$) ion-density waves but also with each ionization

burst revealing a plasma environment rich in low-frequency turbulent behavior. Future experiments with an even more advanced version of this HDLP (plasma properties sampled up to 1 MHz) are underway to probe the magnetized very-near-field HET plasma where anomalous cross-field electron mobility has confounded the theory of electron confinement for decades. Providing high-spatial and temporal resolution measurements with a simple design and theory of operation, the HDLP is an invaluable diagnostic tool that could play an important role in understanding low-frequency plasma turbulence.

¹H. M. Mott-Smith and I. Langmuir, *Phys. Rev.* **28**, 727 (1926).

²M. A. Lieberman and A. J. Lichtenberg, *Principles of Plasma Discharges and Materials Processing* (Wiley, New York, 2005).

³J. D. Swift and M. J. R. Schwar, *Electrical Probes for Plasma Diagnostics* (Elsevier, New York, 1970).

⁴F. F. Chen, *Plasma Diagnostic Techniques*, edited by R. H. Huddlestone (Academic, New York, 1965).

⁵N. Hershkowitz, *Plasma Diagnostics* (Academic, San Diego, 1989), Vol. 1, p. 113.

⁶R. B. Lobbia and A. D. Gallimore, "Temporal limits of a rapidly swept Langmuir probe," *Phys. Plasmas* (to be published).

⁷P. C. Liewer, J. M. McChesney, S. J. Zweben, and R. W. Gould, *Phys. Fluids* **29**, 309 (1986).

⁸R. Balbin, C. Hidalgo, M. A. Pedrosa, I. Garcia-Cortes, and J. Vega, *Proceedings of the Ninth Topical Conference on High Temperature Plasma Diagnostics* (AIP, Santa Fe, NM, 1992), pp. 4605–4607.

⁹L. Giannone, R. Balbin, H. Niedermeyer, M. Endler, G. Herre, C. Hidalgo, A. Rudyj, G. Theimer, and Ph. Verplanke, *Phys. Plasmas* **1**, 3614 (1994).

¹⁰G. Chiodini, C. Riccardi, and M. Fontanesi, *Rev. Sci. Instrum.* **70**, 2681 (1999).

¹¹M. Schubert, M. Endler, and H. Thomsen, *Rev. Sci. Instrum.* **78**, 053505 (2007).

¹²T. F. Yang, Q. X. Zu, and P. Liu, *Rev. Sci. Instrum.* **66**, 3879 (1995).

¹³L. Albarède, S. Mazouffre, A. Bouchoule, and M. Dudeck, *Phys. Plasmas* **13**, 063505 (2006).

¹⁴E. Y. Choueiri, *Phys. Plasmas* **8**, 1411 (2001).

¹⁵R. B. Lobbia, T. M. Liu, and A. D. Gallimore, Proceedings of the Sixth Modeling and Simulation/Fourth Liquid Propulsion/Third Spacecraft Propulsion Joint Subcommittee JANNAF Meeting, SPS-III-36, 2008.

¹⁶J. M. Fife, M. Martinez-Sanchez, and J. Szabo, Proceedings of the 33rd AIAA/ASME/SAE/ASEE Joint Propulsion Conference and Exhibit, 1997, Paper No. AIAA-97-3052.